Evidence of Recent Thrust Faulting on the Moon Revealed by the Lunar Reconnaissance Orbiter Camera

Thomas R. Watters, *et al.*

Science **329**, 936 (2010);
DOI: 10.1126/science.1189590

References and Notes

1. M. Haruta, *CATTECH* **6**, 102 (2002).
2. M. Haruta, *Catal. Today* **36**, 153 (1997).
3. M. Valden, X. Lai, D. W. Goodman, *Science* **281**, 1647 (1998).
4. M. Valden, S. Pak, X. Lai, D. W. Goodman, *Catal. Lett.* **56**, 7 (1998).
5. B. Yoon *et al.*, *Science* **307**, 403 (2005).
6. K. Coulter, X. P. Xu, D. W. Goodman, *J. Phys. Chem. B* **98**, 1245 (1994).
7. D. Tibiletti, A. Goguet, F. C. Meunier, J. P. Breen, R. Burch, *Chem. Commun.* **2004**, 1636 (2004).
8. G. A. Deluga, J. R. Salge, L. D. Schmidt, X. E. Verykios, *Science* **303**, 993 (2004).
9. D. Andreeva *et al.*, *Catal. Today* **72**, 51 (2002).
10. X. S. Liu, O. Korotkikh, R. Farrauto, *Appl. Catal. A* **226**, 293 (2002).
11. Q. Fu, A. Weber, M. Flytzani-Stephanopoulos, *Catal. Lett.* **77**, 87 (2001).
12. S. Hilaire, X. Wang, T. Luo, R. J. Gorte, J. Wagner, *Appl. Catal. A* **215**, 271 (2001).
13. T. Bunluesin, R. J. Gorte, G. W. Graham, *Appl. Catal. B* **15**, 107 (1998).
14. D. W. Goodman, *Chem. Rev.* **95**, 523 (1995).
15. R. Farrauto *et al.*, *Annu. Rev. Mater. Res.* **33**, 1 (2003).
16. J. M. Schwartz, L. D. Schmidt, *J. Catal.* **138**, 283 (1992).
17. C. Bozo, N. Guilhaume, J.-M. Herrmann, *J. Catal.* **203**, 393 (2001).
18. A. Sepulveda-Escribano, F. Coloma, F. Rodriguez-Reinoso, *J. Catal.* **178**, 649 (1998).
19. D. Kalakkad, A. K. Datye, H. Robota, *Appl. Catal. B* **1**, 191 (1992).
20. S. H. Oh, P. J. Michell, R. M. Siewert, *J. Catal.* **132**, 287 (1991).
21. L. Kundakovic, M. Flytzani-Stephanopoulos, *J. Catal.* **179**, 203 (1998).
22. J. A. Rodriguez *et al.*, *Top. Catal.* **44**, 73 (2007).
23. Z. Yan, S. Chinta, A. A. Mohamed, J. P. Fackler Jr., D. W. Goodman, *J. Am. Chem. Soc.* **127**, 1604 (2005).
24. A. Vijay, G. Mills, H. Metiu, *J. Chem. Phys.* **118**, 6536 (2003).
25. E. Wahlström *et al.*, *Phys. Rev. Lett.* **90**, 026101 (2003).
26. A. Sanchez *et al.*, *J. Phys. Chem. A* **103**, 9573 (1999).
27. J. A. Farmer, J. H. Baricuatro, C. T. Campbell, *J. Phys. Chem. C*, 10.1021/jp104593y (2010).
28. M. Romeo, K. Bak, J. El Fallah, F. Le Normand, L. Hilaire, *Surf. Interface Anal.* **20**, 508 (1993).
29. To our knowledge, it is not possible to grow CeO_{2-x}(111) films in this thickness range (1 to 4 nm) with $x < 0.1$ on Pt(111).
30. J. H. Larsen, J. T. Ranney, D. E. Starr, J. E. Musgrove, C. T. Campbell, *Phys. Rev. B* **63**, 195410 (2001).
31. J. A. Farmer, C. T. Campbell, L. Xu, G. Henkelman, *J. Am. Chem. Soc.* **131**, 3098 (2009).
32. J. A. Venables, *Surf. Sci.* **299–300**, 798 (1994).
33. C. T. Campbell, S. C. Parker, D. E. Starr, *Science* **298**, 811 (2002).
34. S. C. Parker, C. T. Campbell, *Phys. Rev. B* **75**, 035430 (2007).
35. J.-L. Lu, H.-J. Gao, S. Shaikhutdinov, H.-J. Freund, *Surf. Sci.* **600**, 5004 (2006).
36. J. H. Wang, M. L. Liu, M. C. Lin, *Solid State Ion.* **177**, 939 (2006).
37. H.-J. Freund, *Surf. Sci.* **601**, 1438 (2007).
38. L. Giordano, M. Baistrocchi, G. Pacchioni, *Phys. Rev. B* **72**, 115403 (2005).
39. J. A. Farmer, N. Ruzycki, J. F. Zhu, C. T. Campbell, *Phys. Rev. B* **80**, 035418 (2009).
40. D. Ricci, A. Bongiorno, G. Pacchioni, U. Landman, *Phys. Rev. Lett.* **97**, 036106 (2006).
41. D. E. Starr, D. J. Bald, J. E. Musgrove, J. T. Ranney, C. T. Campbell, *J. Chem. Phys.* **114**, 3752 (2001).

42. Supported by the U.S. Department of Energy, Office of Basic Energy Sciences, Chemical Sciences Division, grant DE-FG02-96ER14630, and by, NSF Integrative Graduate Education and Research Traineeship DGE-0504573 from the Center for Nanotechnology, University of Washington (J.A.F.).

Supporting Online Material

www.sciencemag.org/cgi/content/full/329/5994/933/DC1
Materials and Methods
Table S1
References

3 May 2010; accepted 13 July 2010
10.1126/science.1191778

Evidence of Recent Thrust Faulting on the Moon Revealed by the Lunar Reconnaissance Orbiter Camera

Thomas R. Watters,[1]* Mark S. Robinson,[2] Ross A. Beyer,[3,4] Maria E. Banks,[1] James F. Bell III,[5] Matthew E. Pritchard,[6] Harald Hiesinger,[7,8] Carolyn H. van der Bogert,[7] Peter C. Thomas,[9] Elizabeth P. Turtle,[10] Nathan R. Williams[6]

Lunar Reconnaissance Orbiter Camera images reveal previously undetected lobate thrust-fault scarps and associated meter-scale secondary tectonic landforms that include narrow extensional troughs or graben, splay faults, and multiple low-relief terraces. Lobate scarps are among the youngest landforms on the Moon, based on their generally crisp appearance, lack of superposed large-diameter impact craters, and the existence of crosscut small-diameter impact craters. Identification of previously known scarps was limited to high-resolution Apollo Panoramic Camera images confined to the equatorial zone. Fourteen lobate scarps were identified, seven of which are at latitudes greater than ±60°, indicating that the thrust faults are globally distributed. This detection, coupled with the very young apparent age of the faults, suggests global late-stage contraction of the Moon.

Most large-scale crustal deformation on the Moon is directly associated with the nearside mare-filled basins and is expressed as contractional wrinkle ridges and extensional arcuate and linear rilles or graben (*1*, *2*). Basin-radial and basin-concentric wrinkle ridges occur in the basin interiors, whereas graben are found at basin margins and in adjacent highlands. The stresses that form this pattern of deformation are the result of loading from uncompensated mare basalt fill that induces subsidence and downward flexure of the lithosphere (*3*). Lobate scarps are tectonic landforms (*4*–*7*) that, unlike nearside wrinkle ridges and graben, are generally found outside of mare-filled basins in the highlands and are the most common tectonic landform on the farside (*2*). In contrast to basin-related wrinkle ridges and graben, lobate scarps are relatively small-scale structures. They are generally linear or curvilinear asymmetric landforms with relatively steeply sloping scarp faces and are often segmented. Analogous large-scale lobate scarps found on Mercury (*8*–*11*) and Mars (*12*) can have over a kilometer of relief; in contrast, known lunar lobate scarps generally have a maximum relief of <100 m (*2*, *4*–*7*) and proportionately smaller lengths (less than tens of kilometers) (*2*, *7*). Based on their morphology and crosscutting relations, these structures are interpreted to be contractional landforms resulting from low-angle thrust faulting (*4*–*7*, *13*). Estimates of the fault displacement-length scaling relations and the linkage between individual scarp segments further support the interpretation that lobate scarps are the surface expression of shallow thrust faults (*2*). Although many lobate scarps are found in the highlands, some occur in mare basalts and others transition from lobate scarps to wrinkle ridges (*2*, *5*, *14*). Because most previously identified lobate scarps could be easily identified only in high-resolution Apollo Panoramic Camera images (*13*, *15*, *16*), covering only a portion of the lunar equatorial zone, their global spatial distribution was unknown. The Lunar Reconnaissance Orbiter Camera (LROC) Narrow Angle Cameras (NACs) and the Wide Angle Camera (WAC) on the Lunar Reconnaissance Orbiter (LRO) have obtained images of known lobate scarps as well as previously undetected scarps ($n = 14$). NAC high-resolution images (0.5 to 2 m per pixel) and topography derived from NAC stereo images allow the most detailed characterization of the morphology and relief of lunar lobate scarps to date.

The Lee-Lincoln scarp (~20.3°N, 30.6°E), just west of the Apollo 17 landing site in the Taurus-Littrow valley, is a well-known lobate scarp (*17*, *18*) that cuts across the mare basalt-filled valley trend-

[1]Center for Earth and Planetary Studies, Smithsonian Institution, Washington, DC 20560, USA. [2]School of Earth and Space Exploration, Arizona State University, Tempe, AZ 85251, USA. [3]Carl Sagan Center, SETI Institute, Mountain View, CA 94043, USA. [4]NASA Ames Research Center, Moffett Field, CA 94035–0001, USA. [5]Department of Astronomy, Cornell University, Ithaca, NY 14853, USA. [6]Department of Earth and Atmospheric Sciences, Cornell University, Ithaca, NY 14853, USA. [7]Institut für Planetologie, Westfälische Wilhelms-Universität, 48149 Münster, Germany. [8]Department of Geological Sciences, Brown University, Box 1846, Providence, RI 02912, USA. [9]Center for Radiophysics and Space Research, Cornell University, Ithaca, NY 14853, USA. [10]Johns Hopkins University Applied Physics Laboratory, Laurel, MD 20723, USA.

*To whom correspondence should be addressed. E-mail: watterst@si.edu

ing roughly north-south between the prominent north and south highland massifs (Fig. 1A). Topography derived from NAC stereo images of the Taurus-Littrow valley (figs. S1 to S3) indicates that the northern segment of the valley-floor scarp has a maximum relief of ~130 m and a narrow low-relief rise associated with the scarp face (figs. S2 and S3). The rise is more pronounced and has greater relief (~20 m) on the southern segment of the valley-floor scarp. The southern segment of the scarp is also flanked by lobate low-relief foothills with a maximum relief of ~40 m (Fig. 1A and fig. S2). NAC images reveal a previously undetected array of narrow shallow troughs in the back-scarp area, west of the scarp face (Fig. 1B). The small-scale troughs have maximum widths of ~25 m and are typically 100 to 200 m in length. Many of the troughs are shallow, with relatively steeply sloping walls and flat floors. We interpret these troughs to be small-scale fractures and graben, indicating extension of the regolith layer and the underlying mare basalts. These graben are among the smallest-scale tectonic landforms yet observed on the Moon. Assuming that the antithetic normal faults of the graben have equal fault-plane dips of ~60° (which is typical for normal faults) and are rooted at the base of the regolith, the regolith depth is estimated to be on the order of the maximum width of the graben. A depth of ~25 m is consistent with the estimated regolith depth at the Apollo 17 landing site (~10 to 32 m), based on regional seismic profile models (*19*). The orientation of the graben varies from west-northwest to northeast. Thus, some of the graben and fractures are subparallel to the orientation of the scarp, whereas others are nearly perpendicular to the scarp (Fig. 1B). The most likely explanation for the back-scarp fractures and graben is flexural bending of the valley-floor basalts, where bending stresses cause extension and faulting of the upper regolith layer. Thrust faults are often accompanied by small-scale parasitic faults that result from flexural bending and layer-parallel extension (*14*, *20*).

The Lee-Lincoln fault scarp (Fig. 1A) is not confined to the mare basalts of the Taurus-Littrow valley (*4*). To the north, the fault cuts across the contact between the valley basalts and the highlands of North Massif, where it extends up-slope for ~400 m before abruptly changing orientation to the northwest, cutting along-slope for over 5 km. The highlands scarp face is about 1 km from the valley floor along much of its length and has a maximum relief of ~5 m (fig. S4).

NAC images of the farside highlands Mandel'shtam scarp (~6.9°N, 161°E), first identified in Apollo Panoramic Camera images (*7*), show that the scarp face is characteristically lobate (Fig. 2A). Like the Lee-Lincoln scarp, Mandel'shtam has subsidiary scarps that form low-relief foothills along some segments. The north-south–trending scarp consists of several segments with a total length of ~12 km. It is one of a series of scarps that occur in the area near Mandel'shtam crater (*7*). NAC images show that the northern terminus of Mandel'shtam scarp appears to be made up of a complex series of small scarps (Fig. 2A). These small scarps are interpreted to be the surface expression of splay faults.

So far, 14 previously unknown lobate scarps have been revealed in NAC images (table S1). These scarps occur in highland material. The northernmost scarp, Rozhdestvenskiy-1, is found on a ledge of rim material along the northern wall of the 42-km-diameter Rozhdestvenskiy crater (~87.5°N, 211.7°E). The east-west–trending scarp has a minimum length of ~5 km and has forefront subsidiary low-relief scarps (Fig. 2B). The Rozhdestvenskiy-1 scarp terminates to the west at the rim of a ~330-m-diameter impact crater. The smallest of the previously unknown lobate scarps is located in the floor material of Slipher crater. This scarp (~48.3°N, 160.5°E) is divided into several segments and is only ~3 km in length (Fig. 2C). The western terminus of the east-west–trending Slipher scarp, like the northern terminus of the Mandel'shtam scarp, consists of a series of splay faults expressed by multiple scarp segments. The vergent side of some of these small fault segments is reversed from south- to north-facing (Fig. 2C). Splay faults are not restricted to the ends of lobate scarps. A previously unknown scarp (~74°S, 8.8°E) located near Simpelius crater has a northeast-trending splay fault that intersects the roughly east-west–trending main scarp at an acute angle (Fig. 2D). The western segment of the Simpelius scarp has multiple terraces that may be the expression of imbricate thrust faulting (Fig. 2D). Multiple terraces suggestive of imbricate faults are associated with other previously known lunar lobate scarps (*2*). The southernmost previously unknown lobate scarp (~86.3°S, 54.7°E) is found near Shoemaker crater. The northern segment of the north-northwest–trending scarp appears to have relatively high relief and a steeply sloping scarp face (Fig. 2E). The scarp cuts along a roughly NW-SE–oriented linear fabric and across an orthogonal NE-SW–oriented fabric in the regolith.

The majority of the previously known lunar scarps are located in the equatorial zone (Fig. 3). Only 20% of the surface of the Moon was imaged by the Panoramic Cameras. It is likely that less than 10% of this coverage had lighting geometry optimal for detecting the small-scale lobate scarps (*2*, *7*). Of the 14 lobate scarps detected in NAC images, seven occur at latitudes greater than ±60° (Fig. 3 and table S1). Three of these scarps, Shoemaker and Rozhdestvenskiy-1 and -2, are located very near the poles. Apparent gaps in the longitudinal distribution of the scarps detected with the NACs, particularly in the equatorial zone, are probably due to limited image coverage in those regions at the time of the survey. The occurrence of previously undetected lobate scarps at high lunar latitudes, along with the distribution of the mid- and low-latitude scarps on both the nearside and farside, suggests that the thrust faults are globally distributed (Fig. 3).

Lobate scarps appear to be very young, among the youngest tectonic landforms on the Moon (*2*, *7*, *13*). NAC images of known and previously unknown scarps reveal crosscutting relations with small-diameter impact craters. The North Massiff segment of Lee-Lincoln scarp crosscuts impact craters with diameters as small as ~7 m (Fig. 4A). Mandel'shtam scarp crosscuts impact

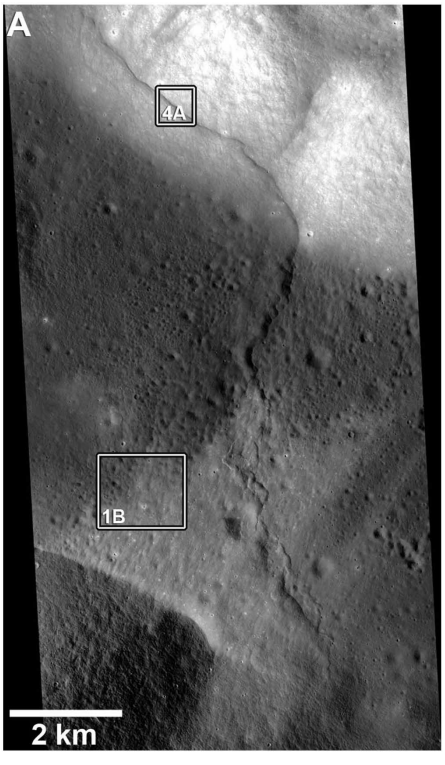

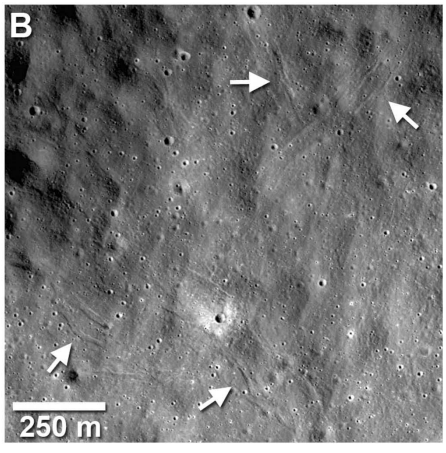

Fig. 1. The Lee-Lincoln scarp in the Taurus-Littrow valley. (**A**) The lobate scarp deforms mare basalts in the Taurus-Littrow valley and extends into the highlands of North Massif where it cuts up- and along-slope (LROC NAC image frame M104318871LE). (**B**) Small narrow troughs in the back-scarp area of the Lee-Lincoln scarp (white arrows). The figure location is shown in (A) (LROC NAC image frame M104318871LE).

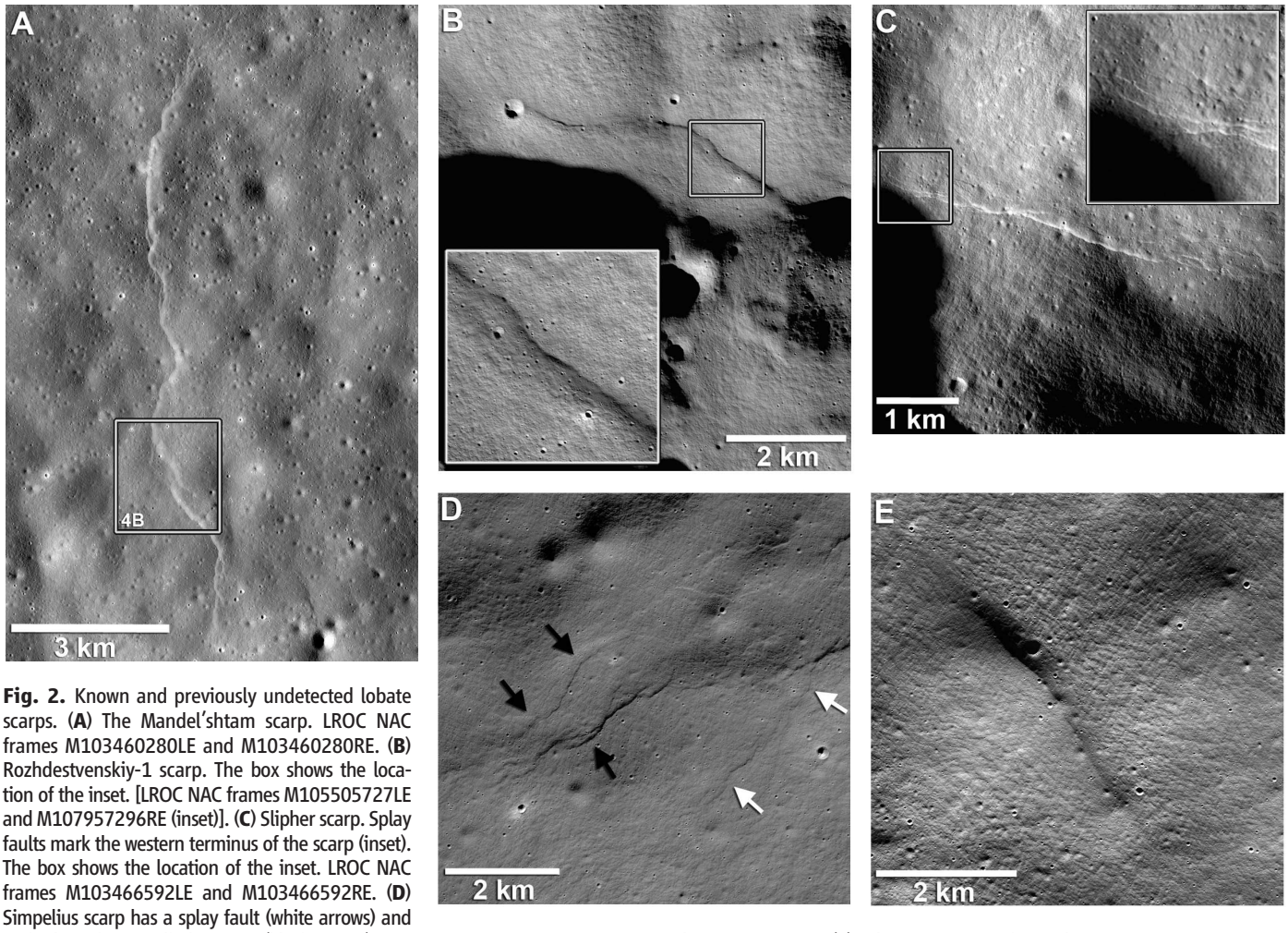

Fig. 2. Known and previously undetected lobate scarps. (**A**) The Mandel'shtam scarp. LROC NAC frames M103460280LE and M103460280RE. (**B**) Rozhdestvenskiy-1 scarp. The box shows the location of the inset. [LROC NAC frames M105505727LE and M107957296RE (inset)]. (**C**) Slipher scarp. Splay faults mark the western terminus of the scarp (inset). The box shows the location of the inset. LROC NAC frames M103466592LE and M103466592RE. (**D**) Simpelius scarp has a splay fault (white arrows) and multiple fault-controlled terraces (black arrows). LROC NAC frames M106807247LE and M106807247RE. (**E**) Lobate scarp near Shoemaker crater. LROC NAC frames M108891721LE and M108891721RE.

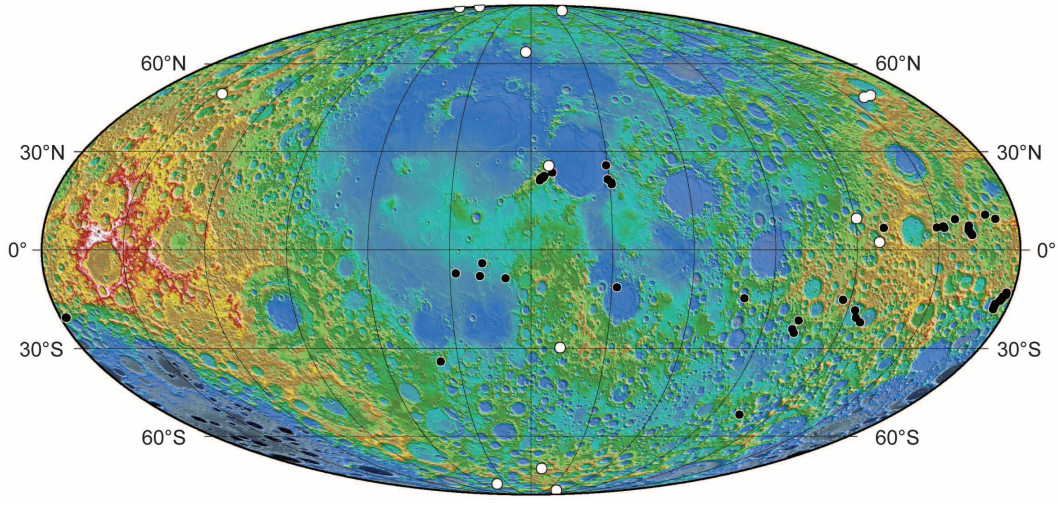

Fig. 3. The spatial distribution of previously known (black dots) and previously unknown (white dots) lobate scarps on the Moon. The distribution of most of the previously known lobate scarps correlates with the limited Apollo Panoramic Camera coverage of the equatorial region. Lobate scarp locations are plotted on a shaded relief map merged with the Lunar Orbiter Laser Altimeter global 64-pixel-per-degree topographic model.

craters of various scales and with various states of degradation (Fig. 4B). Assigning absolute ages to scarps from crater counts is challenging, because they are structural elements that have a limited spatial extent. An upper bound on the age of the scarp can be estimated based on the ages of the stratigraphic units containing crosscut craters. The crosscut craters are <50 m in diameter and from estimates of relative ages of lunar craters with various diameters and degrees of degradation, craters 50 m in diameter or smaller are Copernican in age (*21*). The absolute age of the base of the Copernican is estimated to be ~800 ± 15 million years (if defined by the age of Copernicus crater) (*22*). Thus, the lunar scarps described here are inferred to be <1 billion years old. This age is consistent with the upper-bound age of lobate scarps estimated by Binder and Gunga (*7*). The

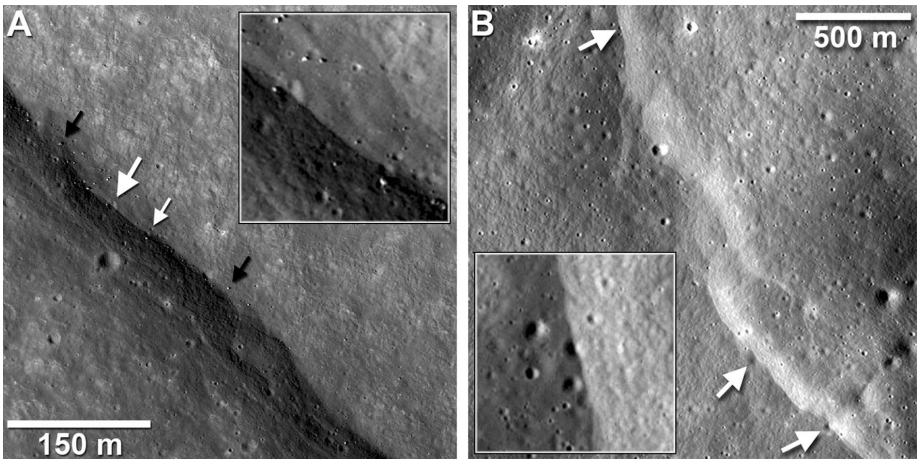

Fig. 4. Crosscutting relations between lobate scarps and impact craters. (**A**) The Lee-Lincoln scarp in North Massif crosscuts an ~12-m-diameter impact crater (large white arrow and inset) and a ~7-m-diameter crater (small white arrow and inset). Boulders are found along the scarp face (black arrows). The figure location is shown in Fig. 1A. (LROC NAC frame M119652859LE.) (**B**) Degraded ~40-m-diameter craters (lower white arrows) and a ~20-m-diameter crater (upper white arrow and inset) are crosscut by the Mandel'shtam scarp. The figure location is shown in Fig. 2A. LROC NAC frames M103460280LE and M103460280RE.

most compelling evidence for a very young age for the lobate scarps is their morphologically crisp, undegraded appearance, transected and disturbed meter-scale impact craters, and a lack of superimposed of large-diameter (>400 m) impact craters.

A major constraint on the initial temperature and thermal evolution of the Moon are estimates of radial contraction (*23*–*26*). The lack of distributed large-scale lobate scarp thrust faults such as those on Mercury that express significant radial contraction argues against secular cooling of a completely molten early Moon (*24*, *25*). Alternatively, the lack of large-scale thrust faults (scarps >100 km in length and with >500 m of relief) may be due to the accommodation of significant contractional strain by the near-surface regolith and an underlying pervasively fractured zone (*27*). The relatively young, globally distributed population of small-scale thrust faults described here, however, may be evidence of late-stage radial contraction of the Moon.

Alternatively, substantial tidally induced stresses in the Moon, a tidally locked satellite undergoing orbital recession, may have been generated from relaxation of an early tidal bulge (*28*). The resulting stresses are expected to cause contraction and thrust faulting in the region around the sub-Earth point and its antipode and extension and normal faulting at the poles (*28*, *29*). This predicted pattern is not consistent with the observed spatial distribution of lobate scarps. Tidal stresses raised solely by Earth are another possible source of global stress; however, their magnitude (a maximum of tens of kilopascals) (*30*) is probably too low to initiate thrust faulting (*31*). However, tidal stresses are a likely component of the total stress that formed the thrust faults.

The areal contractional strain estimated with the displacement-length (*D*-*L*) scaling relation of previously known lobate scarps (*2*), with an updated *D*-*L* value for the Lee-Lincoln scarp, is ~0.01% (*32*). This estimated contractional strain, extrapolated to the entire surface, is equivalent to a radius change of ~100 m and corresponds to isotropic stresses due to radial contraction of <10 MPa (*2*). The detection of previously unknown lobate scarps at high latitudes is consistent with global extrapolation of the regionally derived contractional strain.

Thermal history models for either a nearly or totally molten early Moon, or an early Moon with an initially hot exterior and magma ocean that maintained a cool interior, predict late-stage compressional stresses in the upper lunar crust and lithosphere (*6*, *24*, *25*, *33*–*35*). The initially totally molten model predicts stresses of up to 350 MPa (*7*, *33*). Near-surface compressional stresses of this magnitude might be expected to form a population of thrust-fault scarps comparable in scale to the lobate scarps found on Mercury. Conversely, magma ocean thermal models that limit the change in lunar radius to about ±1 km in the past 3.8 billion years (since the end of the period of late heavy bombardment) predict compressional stresses of ~100 MPa or less (*24*, *33*). Although a more accurate estimate of the contractional strain expressed by the lobate scarps remains to be determined, the value given here may only be a lower limit if substantial horizontal shortening has not been manifested (*27*). However, even if the contractional strain is greater by a factor of 2, the compressional stress due to radial contraction is only on the order of ~15 MPa. Thus, in the absence of substantial unexpressed contractional strain, the observations reported here are consistent with thermal history models that predict low-level compressional stresses and relatively small changes (1 km or less) in lunar radius. The relatively young age of the faults suggests that they formed during a recent episode of lunar radial contraction. Earlier episodes of radial contraction probably resulted in other populations of small-scale thrust faults that are expected to be heavily degraded and as yet unrecognized.

References and Notes

1. D. E. Wilhelms, *U.S. Geol. Surv. Prof. Pap.* **1348**, 302 (1987).
2. T. R. Watters, C. L. Johnson, in *Planetary Tectonics*, T. R. Watters, R. A. Schultz, Eds. (Cambridge Univ. Press, New York, 2010), pp. 121–182.
3. A. M. Freed, H. J. Melosh, S. C. Solomon, *J. Geophys. Res.* **106**, 20603 (2001).
4. K. A. Howard, W. R. Muehlberger, *NASA Spec. Publ.* **SP-330**, 31 (1973).
5. B. K. Lucchitta, *Geochim. Cosmochim. Acta* **3** (suppl.), 2761 (1976).
6. A. B. Binder, *Earth Moon Planets* **26**, 117 (1982).
7. A. B. Binder, H.-C. Gunga, *Icarus* **63**, 421 (1985).
8. R. G. Strom, N. J. Trask, J. E. Guest, *J. Geophys. Res.* **80**, 2478 (1975).
9. T. R. Watters *et al.*, *Earth Planet. Sci. Lett.* **285**, 283 (2009).
10. S. C. Solomon *et al.*, *Science* **321**, 59 (2008).
11. T. R. Watters, F. Nimmo, in *Planetary Tectonics*, T. R. Watters, R. A. Schultz, Eds. (Cambridge Univ. Press, New York, 2010), pp. 15–80.
12. T. R. Watters, *J. Geophys. Res.* **108**, 5054 (2003).
13. P. H. Schultz, *Moon Morphology: Interpretations based on Lunar Orbiter Photography* (Univ. of Texas Press, Austin, TX, 1976).
14. T. R. Watters, *J. Geophys. Res.* **93**, 10236 (1988).
15. T. K. Mattingly, F. El-Baz, R. A. Laidley, *NASA Spec. Publ.* **SP-315**, 28-1 (1972).
16. H. Masursky, G. W. Colton, F. El-Baz, *NASA Spec. Publ.* **SP-362**, 255 (1978).
17. H. H. Schmitt, E. A. Cernan, *NASA Spec. Publ.* **SP-330**, 5-1 (1973).
18. D. H. Scott, *NASA Spec. Publ.* **SP-330**, 31-25 (1973).
19. M. R. Cooper, R. L. Kovach, J. S. Watkins, *Rev. Geophys. Space Phys.* **12**, 291 (1974).
20. J. B. Plescia, M. P. Golombek, *Geol. Soc. Am. Bull.* **97**, 1289 (1986).
21. N. J. Trask, *U.S. Geol. Surv. Prof. Pap.* **750-D**, D138 (1971).
22. D. Stöffler, G. Ryder, *Space Sci. Rev.* **96**, 9 (2001).
23. G. J. F. MacDonald, *Planet. Space Sci.* **2**, 249 (1960).
24. S. C. Solomon, J. Chaiken, *Proc. Lunar Sci. Conf.* **7**, 3229 (1976).
25. S. C. Solomon, in *Origin of the Moon*, W. K. Hartmann, R. J. Phillips, G. J. Taylor Eds. (Lunar and Planetary Institute, Houston, TX, 1986), pp. 311–329.
26. C. K. Shearer *et al.*, *Rev. Mineral. Geochem.* **60**, 365 (2006).
27. M. E. Pritchard, D. J. Stevenson, in *Origin of the Earth and Moon*, R. Canup, K. Righter Eds. (Univ. of Arizona Press, Tucson, AZ, 2000), pp. 179–196.
28. H. J. Melosh, *Icarus* **43**, 334 (1980).
29. G. C. Collins *et al.*, in *Planetary Tectonics*, T. R. Watters, R. A. Schultz, Eds. (Cambridge Univ. Press, New York, 2010), pp. 264–350.
30. R. C. Weber, B. G. Bills, C. L. Johnson, *J. Geophys. Res.* **114**, E05001 (2009).
31. D. L. Turcotte, G. Schubert, *Geodynamics: Application of Continuum Physics to Geological Problems* (Cambridge Univ. Press, New York, 2002).
32. This value of the contractional strain assumes fault-plane dips of 30°. The estimated displacements for eight previously known scarps determined by Watters and Johnson (*2*) range from ~12 to 108 m (corresponding to a range of horizontal shortening of ~10 to 92 m). The Lee-Lincoln scarp has a displacement of ~260 m (horizontal shortening of ~225 m), estimated with the NAC stereo-derived Digital Terrain Model (figs. S1 and S3).

33. S. C. Solomon, J. W. Head, *J. Geophys. Res.* **84**, 1667 (1979).
34. A. B. Binder, M. A. Lange, *Moon* **17**, 29 (1977).
35. A. B. Binder, in *Origin of the Moon*, W. K. Hartmann, R. J. Phillips, G. J. Taylor Eds. (Lunar and Planetary Institute, Houston, TX, 1986), pp. 425–433.
36. We thank the three anonymous reviewers for helpful comments that improved the manuscript. We gratefully acknowledge the Lunar Orbiter Laser Altimeter team for the lunar topographic model and the LRO and LROC engineers and technical support personnel. This work was supported by the LRO Project, NASA grants NNX08AM73G and NNG07EK00C, and through Deutsches Zentrum für Luft- und Raumfahrt grant 50 OW 0901.

Supporting Online Material
www.sciencemag.org/cgi/content/full/329/5994/936/DC1
SOM Text
Figs. S1 to S4
Table S1

15 March 2010; accepted 8 July 2010
10.1126/science.1189590

Drought-Induced Reduction in Global Terrestrial Net Primary Production from 2000 Through 2009

Maosheng Zhao* and Steven W. Running

Terrestrial net primary production (NPP) quantifies the amount of atmospheric carbon fixed by plants and accumulated as biomass. Previous studies have shown that climate constraints were relaxing with increasing temperature and solar radiation, allowing an upward trend in NPP from 1982 through 1999. The past decade (2000 to 2009) has been the warmest since instrumental measurements began, which could imply continued increases in NPP; however, our estimates suggest a reduction in the global NPP of 0.55 petagrams of carbon. Large-scale droughts have reduced regional NPP, and a drying trend in the Southern Hemisphere has decreased NPP in that area, counteracting the increased NPP over the Northern Hemisphere. A continued decline in NPP would not only weaken the terrestrial carbon sink, but it would also intensify future competition between food demand and proposed biofuel production.

Terrestrial ecosystems are a major sink in the global carbon cycle, sequestering carbon and slowing the increasing CO_2 concentration in the atmosphere (*1*). Terrestrial net primary production (NPP), the initial step of the carbon cycle in which carbon is fixed as biomass, increased from 1982 through 1999, in part due to eased climatic constraints on plant growth (*2*). The World Meteorological Organization (WMO), National Oceanic and Atmospheric Administration (NOAA), and NASA all reported that 2000 to 2009 was the warmest decade since instrumental measurements of temperatures began in the 1880s (*3*). We questioned whether the warming climate of the past decade continued to increase NPP, or if different climate constraints were more important.

Between 2000 and 2008, CO_2 emissions from fossil fuel combustion continued to increase at a rate consistent with the average of the highest-emissions family of scenarios, A1FI, used by the Intergovernmental Panel on Climate Change in the Fourth Assessment (*1*). Carbon-budget methods show that the land is becoming a stronger carbon sink, whereas large uncertainties exist in the partitioning of ocean and land carbon-sink components (*1*, *4*). Satellite data can generally provide realistic information on vegetation dynamics, including land cover change (*5*, *6*), disturbances, and recovery (*7*), which may help to reduce uncertainties in carbon-budget estimates. In this study, we investigate terrestrial NPP and climate variability over the past decade (2000 to 2009) by analyzing satellite data from the Moderate Resolution Imaging Spectroradiometer (MODIS) on board NASA's Terra satellite and global climate data.

We used the global MODIS NPP algorithm (*8*) [see supporting online material (SOM) text S1] to examine spatially explicit NPP changes from 2000 through 2009. We used collection 5 (C5) 8-day composite 1-km fraction of photosynthetically active radiation (FPAR) and leaf area index (LAI) data from the MODIS sensor (*9*) as remotely sensed vegetation property dynamic inputs to the algorithm. Data gaps in the 8-day temporal MODIS FPAR/LAI caused by cloudiness were filled with information from accompanying quality-assessment fields (SOM text S2) (*10*). For daily meteorological data required to drive the algorithm, we used a reanalysis data set from National Center for Environmental Prediction (NCEP) (SOM text S3) (*11*). A Palmer Drought Severity Index (PDSI) (*12*) at 0.5° resolution was used as a surrogate of soil moisture (*13*) to measure environmental water stress by combining information from both evaporation and precipitation (SOM text S4). A lower PDSI generally implies a drier climate.

Global NPP slightly decreased for the past decade by −0.55 Pg C (Fig. 1). Interannual variations of the global NPP were negatively correlated with the global atmospheric CO_2 growth rates (correlation coefficient $r = -0.89$, $p < 0.0006$) (Fig. 1) (*14*), suggesting that global terrestrial NPP is a major driver of the interannual CO_2 growth rate. Carbon isotopic measurements have indicated that the exchange of CO_2 with terrestrial ecosystems is the dominant cause of the CO_2 interannual growth rate (*15*). Though NPP is a part of carbon exchange between the land and atmosphere, the strong correlation may imply that the process of heterotrophic respiration depends ultimately on the substrate supply from NPP (*16*),

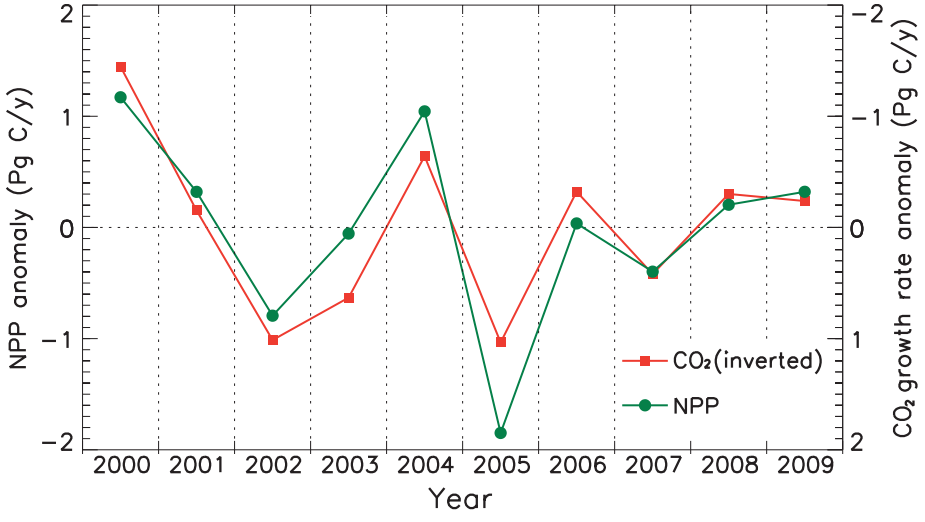

Fig. 1. Interannual variations from 2000 through 2009 in anomalies of annual total global terrestrial NPP (green circles) and inverted global atmospheric CO_2 annual growth rate [red squares and (*14*)]. Global average annual total NPP is 53.5 Pg C/yr.

Numerical Terradynamic Simulation Group, Department of Ecosystem and Conservation Sciences, the University of Montana, Missoula, MT 59812, USA.

*To whom correspondence should be addressed. E-mail: zhao@ntsg.umt.edu